Separation and Purification Technology 323 (2023) 124487

Contents lists available at ScienceDirect

Separation and Purification Technology

journal homepage: www.elsevier.com/locate/seppur

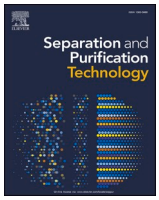

Uptake and separation of rare earth elements and late transition metal cations by nanoadsorbent grafted with diamino ligands

Marijana Lakić [a], Troy C. Breijaert [a], Geoffrey Daniel [b], Fredric G. Svensson [c], Vadim G. Kessler [a], Gulaim A. Seisenbaeva [a,*]

[a] Department of Molecular Sciences, Biocentrum, Swedish University of Agricultural Sciences, Almas Allé 5, Box 7015, SE-750 07 Uppsala, Sweden
[b] Department of Forest Biomaterials and Technology, Swedish University of Agricultural Sciences, Vallvägen 9C-D, SE-756 51 Uppsala, Sweden
[c] Department of Materials Science, Solid State Physics, Box 35, Ångströmlaboratoriet, Lägerhyddsvägen 1, Uppsala University, SE-751 03 Uppsala, Sweden

ARTICLE INFO

Keywords:
Critical metals
Rare Erath Elements
Late Transition metals
Recycling
Molecular interaction model

ABSTRACT

Recycling of magnetic materials based on Rare Earth Elements (REE) is of major interest in the view of growing clean energy production and transportation. One of the major challenges in its realization is the need to separate smaller amounts of Late Transition Metals (LTM) from REE. Hybrid adsorbents are very attractive in finding such a solution. Here, novel silica-based nanoadsorbents were synthesized by grafting the surface of dense silica nanoparticles with a diamino functional ligand grafted via an arene linker to improve selectivity towards LTM. The produced adsorbent materials were characterized using SEM, TEM, AFM, XPS, FTIR, and TGA in its pure form and by DLS in suspension, and tested for the adsorption and separation of LTM (Co^{2+} and Ni^{2+}) and REE (Sm^{3+} and Nd^{3+}) in single and mixed solutions. Prepared organo-silica material showed rapid uptake of all tested cations with higher affinity towards LTM. Adsorption capacities reached values of 1.18–1.45 mmol/g for Co^{2+} and Ni^{2+}, respectively, with a 1:1 metal-to-ligand stoichiometry for Ni cations. Investigation of reusability demonstrated the potential of the prepared materials as an environmentally friendly alternative in specific separation of LTM to conventional separation techniques. Investigations of the molecular structures of the Ni^{2+} complex with the selected molecular function and of Co^{3+} with a closely related tris-aminoethyl amine ligand in combination with XPS data for corresponding surface complexes helped explaining the molecular mechanisms for adsorption and desorption of the LTM cations.

1. Introduction

Rapid population growth and accelerated advances in industrialization and urbanization and overconsumption of fossil fuels are coupled with increase emissions of climate-changing greenhouse gases [1,2]. The rise of green (low-carbon) technology with smart electrical grid programs substituting fossil-driven vehicle parks, and vehicle-to-grid technology are among the new tools for successful decarbonization and preventing further global temperature rises. Many of these fast-growing technologies, in particular, wind turbines and electric vehicles, utilize rare earth elements (REE) sourced via mining from a monopolized supply chain where there is increased demand [3–7]. Principal components in these applications are permanent magnets, i.e., FeNdB and CoSm magnets, where REE, neodymium (Nd) and samarium (Sm) are represented together with late transition metals (LTM) [8]. Scarce REE and LTM, especially copper, nickel, cobalt, platinum, and silver, are predicted to face market pressure as the production of green energy technologies intensifies [9,10]. To solve the supply issue and to meet future demands, there is a need to exploit recycling schemes for the recovery of REE from secondary resources with an emphasis on their selective separation from LTM, as a green alternative to mining and processing of solid REE [11–13]. In the recycling, the separation of REE from LTM represents thus a principal challenge. While iron can easily be separated by controlled increase in pH, separation of Co, Ni and Cu requires application of advanced approaches including fractional crystallization [14], solvent extraction [15–16] or use of solid adsorbents [17]. The drawback of the crystallization approach is the need in multi-step procedures. The solvent extraction uses large amounts of organic solvents and hazardous extractants. The solid adsorption is generally considered as a greener alternative.

* Corresponding author at: Department of Molecular Sciences, Biocentrum, Swedish University of Agricultural Sciences, Almas Allé 5, Box 7015, SE-750 07 Uppsala, Sweden.
E-mail address: gulaim.seisenbaeva@slu.se (G.A. Seisenbaeva).

https://doi.org/10.1016/j.seppur.2023.124487
Received 7 May 2023; Received in revised form 26 June 2023; Accepted 30 June 2023
Available online 1 July 2023

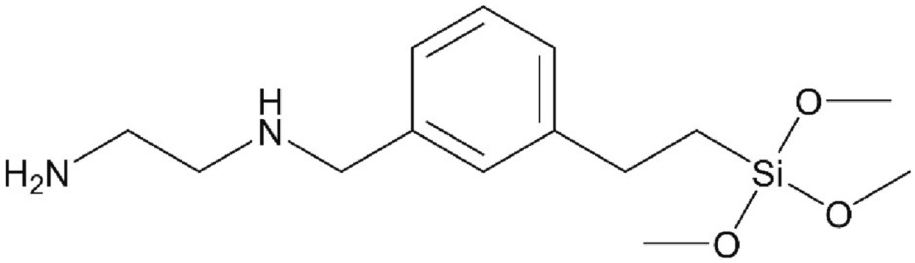

Fig. 1. Ligand N-(aminoethylaminomethyl)phenethyltrimethoxysilane.

Current hydrometallurgical recycling techniques for permanent magnets include acid leaching using inorganic acid (HCl, H_2SO_4, or HNO_3) and subsequent separation methods, such as several precipitation steps or liquid phase extraction (solvent extraction processes, ionic liquid extraction) [18]. Liquid phase extraction uses large volumes of reagents and solvents that can release volatile organic compounds (VOC), produce toxic and flammable wastes, and requires repetition of cycles to achieve appropriate metal purity due to the difficulties of REE separation from LTM. Additional disadvantages are poor contact between the extractant and desired elements and the formation of an unwanted third (heavy organic) phase due to the splitting of the organic phase into two layers, which can affect the efficiency of the extraction process, requiring additional separation steps before the extraction can be considered complete [19,20]. Solid-liquid extraction using adsorbents compensate for these disadvantages [21] and enables rapid uptake of the aqueous metals and easy separation of the treated solution from the solid sorbent [11]. In this context, adsorption represents an environmental, eco-friendly, and non-expensive alternative to the use of liquid phase extraction and meets the requirements of "Circular economy schemes" proposed by the European Union for resource recovery from solid waste or wastewater to solve scarce resource problematics, realizing the "waste to product" concept [22].

Next-generation adsorbents - nanoadsorbents with high adsorption capacity and selectivity - have gained the science community's interest [23–32]. These properties arise from the increased surface area and reactivity of nanoadsorbents compared to their bulk counterparts. A further important characteristic is their possibility for surface functionalization allowing the grafting of ligands targeting specific metal cations or contaminants. In addition to these characteristics, superior nanoadsorbents are easily dispersed in liquid media, chemically stable, uniform in size, cheap and reusable [33–37].

In our search for separation between REE and LTM, we turned to the application of polyamino ligands. It is well-known that such ligands have high affinity for LTM cations, forming stable complexes in neutral and basic medium that potentially can be destroyed at rather low pH, releasing hydrated LTM cations [38]. At the same time, it is well known that complexation between REE and polyamino ligands can be followed only in non-aqueous medium and not in water [39]. In our recent studies, we demonstrated that tris(aminoethyl)-amine, an example of polyamino ligand displayed different mechanisms in interacting with LTM and REE cations respectively. While complexation was observed with LTM in a pH-neutral medium, REE produced hydroxides as result of hydrolysis of their cations with precipitation of hydroxides and the formation of protonated ammonium salts [40]. This difference could be traced in lower adsorption of REE cations compared to LTM, on a biopolymer adsorbent grafted with tris(2-aminoethyl)-amine as well as easier desorption.

In the present work, we aimed to further increase selectivity of the interaction, and opted for introduction of an aromatic ring in direct proximity to a diamino function. This could result, either in improved control of hydrophilicity/hydrophobicity of the surface via ligand self-organization through π-stacking, or create more specific coordination surrounding for LTM with ability to distinguish between Ni^{2+} and Co^{2+} via possibility of dπ -pπ contribution. In the current study, the synthesis and characterization of hybrid silica nanoadsorbents, prepared by surface grafting of dense silica nanoparticles of an approximate size of 100 nm, with the commercially available ligand (aminoethylaminomethyl)-phenethyltrimethoxysilane (AEAM-PTMS), featuring the desired structure are presented. To the best of our knowledge, this is the first use of this ligand for selective metal uptake and adsorption. The difference in reactivity of Ni^{2+} and Co^{2+} was revealed via structural studies of molecular model compounds.

2. Experimental methods

2.1. Reagents

Tetraethyl orthosilicate (TEOS, 99 %, CAS No. 78-10-4), ethanol (99.7 %, CAS No. 64-17-5), ammonium hydroxide solution (25 %, CAS No. 1336-21-6), nickel(II) nitrate hexahydrate (94.5-105.5 % (EDTA titration), CAS No.13478-00-7), cobalt(II) nitrate hexahydrate (98 %, CAS No. 10026-22-9), neodymium(III) nitrate hexahydrate (99.9 %, CAS No. 16454-60-7), samarium(III) nitrate hexahydrate (99.9 %, CAS No. 13759-83-6), toluene (≥99.5 %, CAS No. 108-88-3), murexide (≥95 %, CAS No. 3051-09-0), Xylenol orange tetrasodium salt (≥95 %, CAS No. 3618-43-7), ammonium chloride (≥99.5 %, CAS No. 12125-02-9), acetic acid (≥99.7 %, CAS No. 6444-19-7), N-Benzylethylenediamine (97 %, CAS No. 4152-09-4), and Tris(2-aminoethyl) amine (96%, CAS No. 4097-89-6) were purchased from Merck. Nitric acid (65 %, CAS No. 7697-37-2) was purchased from Riedel-de Haën, sodium acetate trihydrate (≥99.0 %, CAS No. 6131-90-4) was purchased from VWR, ethylenediaminetetraacetic acid tetrasodium salt dihydrate (EDTA, 99 %, CAS No. 10378-23-1) was purchased from AppliChem, and aminoethylaminomethyl)phenethyltrimethoxysilane (AEAM-PTMS, 80 %, CAS No: 74113-77-2) was purchased from Gelest.

All chemicals, except toluene, were used as received without further purification. Toluene was dried via a distillation process. For the preparation of all aqueous solutions, Milli-Q water was used.

2.2. Synthesis and characterization of nanoadsorbents

2.2.1. Synthesis of dense silica particles

Dense SiO_2 nanoparticles (NPs) were synthesized using a modified Stöber method as described earlier [41]. Hydrolysis of precursor TEOS was performed in an alcoholic solution using ammonium hydroxide as a catalyst. The reaction mixture consisted of 200 mL 96% ethanol, 35 mL Milli-Q water, and 7.5 mL of 25 % ammonium hydroxide solution and was mixed in a reaction flask at 70 °C and under the nitrogen atmosphere. 11.16 mL of TEOS was added dropwise with a PET syringe supplied with a stainless steel 0.80x80mm needle, stirring the reaction mixture for 2 h. When the reaction stopped, the SiO_2 NPs were centrifuged (12000 rpm, 10 min), washed twice with ethanol (95 %) and three times with Milli-Q water. Particles were dried under nitrogen before further use.

2.2.2. Grafting of silica particles

Prior to the grafting step, dry silica particles were pre-treated with 1 M HNO_3 to enhance the surface grafting onto surface silanol groups [42,17]. 500 mg of dry and acid-pretreated silica particles were dispersed in 20 mL of dry toluene. 1 mL of ligand N-(aminoethylaminomethyl)phenethyltrimethoxysilane (AEAM-PTMS) was then added (see Fig. 1), and the components mixture was kept in a reaction flask equipped with a reflux condenser for 24 h at 80 °C and under nitrogen flow.

2.3. Synthesis of model compounds

To reveal the molecular structure of metal complexes on the surface of prepared nanoadsorbent, we attempted crystallization of the complexes between Ni(II) nitrate and N-aminoethyl aminomethyl benzene ligand in 1: 1, 1: 2 and 1: 3 M ratios and Co(II) nitrate with both N-aminoethyl-aminomethyl benzene and with tris(aminoethyl) amine ligands in in 1: 1 M ratio. Light violet (lilac) coloured crystals were isolated in all cases where Ni^{2+} cation salts were used and proved as the same crystalline material of compound **1**. In the case of Co^{2+} cations, the color of solution turned in all cases greenish brown with formation of a glassy product. The color indicated oxidation of Co(II) into Co(III) with formation of hydroxo complexes. Thus, to avoid hydrolysis of Co(III) species, the pH of the solution was adjusted to 3.0 by addition of nitric acid. The solutions then turned bright red. In the case of N-aminoethyl aminomethyl benzene, only a glassy solid could be isolated, while in the case of tris(aminoethyl) amine, massive crystallization of a single crystalline product compound **2** was observed.

2.4. Physical characterization of obtained adsorbent material

Scanning electron (SEM) micrographs of prepared adsorbent material were obtained using an Hitachi FlexSEM 1000II with acceleration voltage of 5 kV, a spot size 20, and a working distance of 5 mm. For Transmission Electron Microscopy (TEM) experiments, dispersions of adsorbent particles were deposited on holey carbon grids (Pelco® 50 mesh grids: Pitch 508 μm; hole width 425 μm; bar width 83 μm; transmission 70%) and observed using a Philips CM/12 microscope (Thermo Fisher Inc.) fitted with LaB_6 and operated at 100 kV.

Nanoadsorbent's selectivity to metals was characterized by elemental analysis of surfaces using energy-dispersive X-ray spectroscopy (EDS). EDS spectra were obtained using an acceleration voltage of 20 kV, a spot size of 40 and a working distance of 10 mm on the Hitachi FlexSEM 1000II microscope.

Atomic Force Microscope (AFM) images were taken with a Bruker Dimension FastScan instrument using a FastScan-B probe with a nominal tip radius of 5 nm and a scan rate of 1–3 Hz. Gwyddion 2.56 software was used for data processing.

The thermogravimetric analysis (TGA) of samples was carried out using a PerkinElmer Pyris 1 instrument in an air atmosphere at a heating rate of 5°/min in the 25–800 °C interval.

Fourier-transform infrared (FTIR) spectra were recorded as KBr pellets on a PerkinElmer Spectrum 100 instrument from 4000 to 400 cm^{-1}.

Dynamic Light Scattering (DLS) measurements for determination of the particle size and charge (zeta-potential) were carried out with a Malvern Zeta-Sizer Instrument in aqueous dispersions produced by ultrasonication.

X-ray structure determinations. Single-crystal X-Ray Diffraction analysis was performed using a Bruker D8 Quest ECO diffractometer. The data were collected at room temperature in the 2–50.05 2theta range for a full hemisphere using MoKα radiation (λ = 0.71073 Å). *Compound 1*. $C_{18}H_{28}N_6NiO_8$, MW = 515.17 Da, Monoclinic, Space group P2(1)/c, a = 10.206(2), b = 11.324(2), c = 10.377(2) Å, β = 95.145(4)°, V = 1194.4 (4) $Å^3$, Z = 2. The structure was solved by direct methods, obtaining coordinates of the majority of non-hydrogen atoms from the initial solution. The coordinates of the rest of the non-hydrogen atoms were obtained from difference Fourier syntheses. All non-hydrogen atoms were refined first in isotropic and then in anisotropic approximation. The coordinates of hydrogen atoms at the carbon atoms and the terminal nitrogen atom N(1) were obtained by geometric calculation, while those on the solvating water molecule were located in difference Fourier syntheses. All hydrogen atoms were refined in riding approximation bound to corresponding non-hydrogen atoms using temperature factors of these atoms to define the isotropic temperature factors of the hydrogen atoms defined as 1.200 U_{eq} for H-atoms located at C or N atoms and 1.500 U_{eq} for those in the solvating water molecule. The final discrepancy factors were R1 = 0.0951, wR2 = 0.22183 for 1554 observed reflections [I > 2sigma(I)], and R1 = 0.1193 and wR2 = 0.2291 for all 2096 data.

Compound 2. $C_6H_{14}CoN_7O_{10}$, MW = 403.17 Da, Orthorhombic, Space group Pna2(1), a = 25.6816(11), b = 7.2953(3), c = 7.9417(3) Å, Z = 4. The structure was solved by direct methods, obtaining coordinates of the non-hydrogen atoms connected to the cobalt cation from the initial solution. Coordinates of nitrogen and oxygen atoms belonging to the nitrate counterions were located in subsequent difference Fourier syntheses. All non-hydrogen atoms were refined first in isotropic and then in anisotropic approximation. The coordinates of hydrogen atoms at the carbon atoms and the terminal nitrogen atoms N(2), N(3) and N (4) were obtained by geometric calculation, while those on the solvating water molecule were identified in subsequent difference Fourier syntheses. All hydrogen atoms were refined in riding approximation bound to corresponding non-hydrogen atoms using temperature factors of these atoms to define the isotropic temperature factors of the hydrogen atoms defined as 1.200 U_{eq} for H-atoms located at C or N atoms and 1.500 U_{eq} for those in the solvating water molecule. The final discrepancy factors were R1 = 0.0683, wR2 = 0.1904 for 2372 observed reflections [I > 2sigma(I)], and R1 = 0.0727, wR2 = 0.1972 for all 2528 data.

Full details of data collection and structure solution and refinement are available free-of-charge from the Cambridge Crystallographic Data Centre (CCDC) at https://www.ccdc.cam.ac.uk citing the deposition number **2,239,325** for compound **1** and **2,260,061** for compound **2**.

X-ray Photoelectron spectroscopy (XPS) was performed using a Quantera II Scanning XPS Microscope from Physical Electronics equipped with an Al Kα source. For charge compensation a low-energy floodgun, set at 1.0 V and 20.0 μA, was employed. The survey spectra were recorded using a pass energy of 224 eV and a resolution of 0.8 eV, and for the high-resolution spectra a pass energy of 55 eV and 0.1 eV resolution were employed. The samples were suspended in deionized water, dropped on glass slides, and dried under a desktop lamp. The binding energy was calibrated against the C 1 s peak of adventitious carbon at 284.8 eV from a reference sample. The data was treated in the CASA XPS software [43]. The spectra were smoothed using a Savitzky-Golay algorithm with either a 5 or 9-point window.

2.5. Functional characterization of the adsorbent material

2.5.1. Adsorption isotherms

For adsorption experiments, 20 mg of nanoadsorbent was added to a 50 mL falcon tube, followed by the addition of 20 mL of an appropriate metal stock solution with concentrations of 0.5, 1, 2, 3, 4, and 10 mM. After adding $NaNO_3$ solution to retain a constant ionic strength, the samples were left to equilibrate for 48 h before collecting the particles via centrifugation. The pH of initial solution was 7.5 apparently due to protonation of the ligand amino functions. The amount of metal uptake was determined by complexometric titration of the supernatant with 5 mM EDTA. Xylenol orange indicator and 1 M acetate buffer were used for REE (Sm, Nd) determination, and murexide and 1 M ammonia buffer were used for LTM (Co, Ni) determination. The titrations were repeated in triplicates for each sample, and the average value was calculated. The relation between the adsorbed metal and adsorbent mass at a fixed

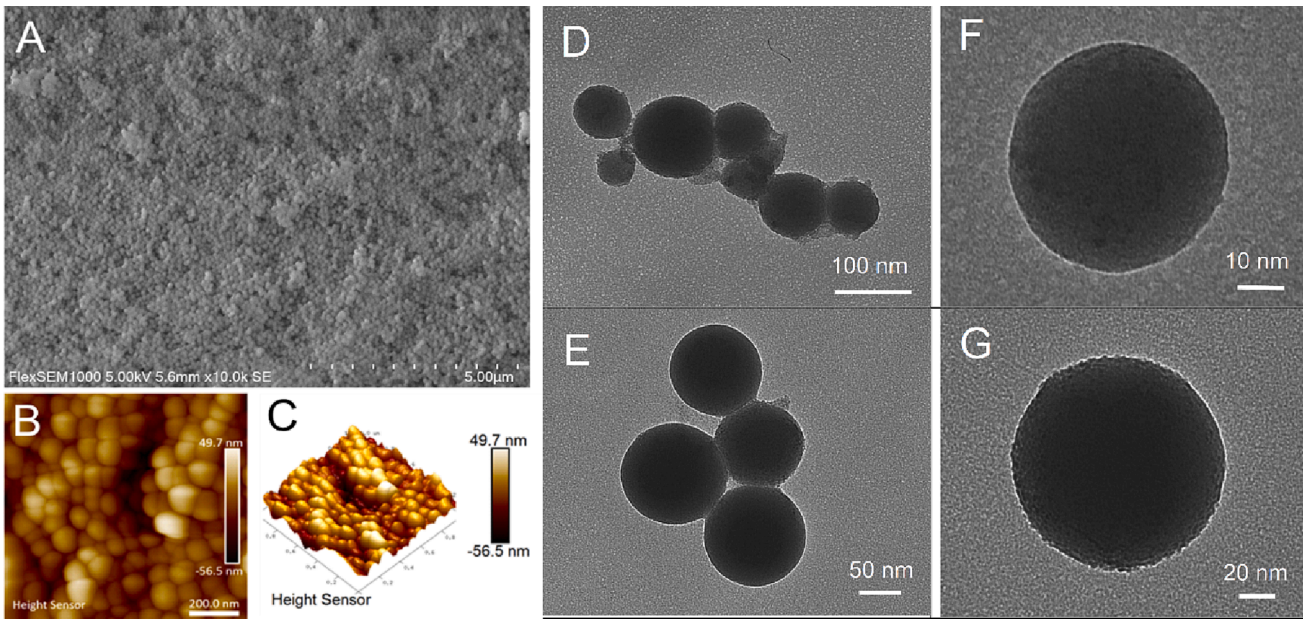

Fig. 2. SEM (A) and AFM (B & C) images of prepared pristine dense silica nanoparticles, and TEM images of D, E: SiO_2-AEAM-PTMS; F, G: SiO_2-AEAM-PTMS + Ni.

temperature are presented as adsorption isotherms. The shape of obtained isotherms provides considerable data regarding the nature of the adsorption process. Adsorption isotherms generally show a plateau at high metal concentrations, corresponding to the saturation of the adsorbent surface. To rationalize the shape of an adsorption isotherm, Langmuir and Freundlich isotherm models are used [44–46].

The Langmuir adsorption isotherm proposes that metal uptake occurs on a homogeneous adsorbent surface by monolayer sorption without interactions between adsorbed molecules. Eq. (1) presents linear and Eq. (2) nonlinear forms of Langmuir isotherm:

$$\frac{C_{ad,e}}{q_{ad,e}} = \frac{1}{q_{max} \times K_L} + \frac{C_{ad,e}}{q_{max}} \tag{1}$$

$$q_{ad,e} = \frac{K_L \times q_{max} \times C_{ad,e}}{1 + K_L \times C_{ad,e}} \tag{2}$$

Reversible and multilayer adsorption on a heterogeneous adsorbent surface is proposed by the Freundlich adsorption isotherm, where the adsorbed amount increases with the concentration in accordance with the following nonlinear (Eq. (3)) and linear equations (Eq. (4)).

$$q_{ad,e} = K_f \times C_{ad,e} \tag{3}$$

$$lnq_{ad,e} = lnK_f + \frac{1}{n} \times lnC_{ad,e} \tag{4}$$

$C_{ad,e}$ denotes the equilibrium concentration of metal ions (mg/L), $q_{ad,e}$ is the amount of metal adsorbed per specific amount of adsorbent (mg/g), q_{max} is the maximum adsorption capacity of adsorbent (mg/g), and K_L is an equilibrium constant that reflects the affinity between the adsorbent and adsorbate (L/mg). The values of q_{max} and K_L were calculated by both linear (from the slope and intercept of the linear plot of $C_{ad}/q_{ad,e}$ versus C_{ad}) and non-linear (by OriginPro 9) methods.

2.5.2. Adsorption kinetics

Adsorption kinetics control the adsorption rate, determining the time required to reach equilibrium for the adsorption process. For adsorption kinetic experiments, 20 mg of grafted silica nanoparticles was suspended in 20 mL of 10 mM metal solution and shaken at RT. Samples were taken at predetermined intervals of 15 min, 30 min, 1 h, 3 h, 6 h, 18 h, and 24 h, and titrated against 5 mM EDTA.

Kinetic models can give information regarding adsorption pathways and probable mechanism involved [47,48]. The tested kinetic models were pseudo-first order, given by Eq. (5), and pseudo-second order, given by Eq. (6):

$$q_{ad,t} = q_{ad,e} \times (1 - e^{-k_1 \times t}) \tag{5}$$

$$q_{ad,t} = \frac{k_2 \times q_{ad,e}^2 \times t}{1 + k_2 \times q_{ad,e} \times t} \tag{6}$$

$q_{ad,t}$ denotes the adsorption capacity in given time (mg/g), $q_{ad,t}$ is the equilibrium adsorption capacity (mg/g), t is the adsorption time (h), k_1 is the constant of pseudo-first-order model (1/min), and k_2 is the constant of pseudo-second-order model (g/mgmin).

2.5.3. Metal selectivity

10 mg of dry particles were equilibrated for 24 h in 10 mL of equimolar (5 mM) aqueous metal mixtures on a shaker at RT. The metal release was done using 1 M HNO_3 for 24 h at RT. The samples were dried under an N_2 atmosphere before metal mapping using EDS.

2.5.4. Desorption and reusability studies

For the desorption test, we studied two different desorption media, HNO_3 with three different concentrations and pH values (pH 0, pH 1, and pH 3) and 10 mM EDTA with pH 4.9. Desorption efficiencies were studied in an equimolar mixture of two (Co/Sm, Ni/Nd, Ni/Co, and Sm/Nd) or with all four tested metals. Reusability studies were carried out by three successive adsorption and desorption steps, using one metal solution (20 mM) in the adsorption step and 1 M HNO_3 as the desorption media. Desorption was carried out for 24 h, mixing the samples on the shaker. Afterwards, the samples were centrifuged (10000 rpm, 10 min), the supernatant collected, neutralized with ammonia to a pH value of 6.5, and titrated with 5 mM EDTA to calculate the amount of desorbed metal.

3. Results and discussion

3.1. Preparation of nanoadsorbents

The morphology of the synthesized material was analyzed by SEM, TEM and AFM techniques, proving the formation of highly uniform spherical particles with an average particle size of 100 nm preserved on

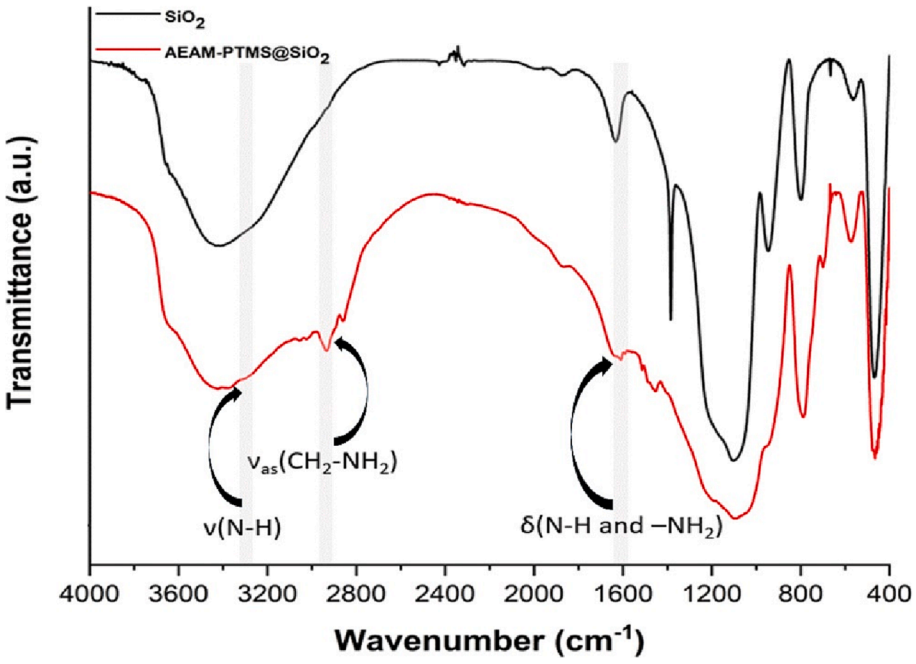

Fig. 3. FTIR spectra of synthesized control and AEAM-PTMS grafted silica particles.

all further steps of treatment, both on ligand grafting and with subsequent adsorption of metal cations (see Fig. 2).

The material produced by ligand grafting contained the required amounts of organics corresponding to monolayer formation. According to the TGA study (see Fig. S1 in Supplementary material), the first step of weight loss corresponding to approximately 3 % was observed at 25–120 °C and occurred due to dehydration of the silica surface and evaporation of the residual organic solvent (dry toluene). Above 120 °C, 16.7 % weight loss was observed until 500 °C, attributed to decomposition of the surface grafted ligand. The losses above 500 °C were related to the carbonization of organic residues on SiO_2 NPs and combustion of the residual carbon. The calculated amount of grafted ligand AEAM-PTMS was estimated from TGA data as 1.47 mmol/g.

The chemical nature of grafting of the ligand was revealed by FTIR (see Fig. 3). The spectra of surface grafted SiO_2 NPs showed characteristic peaks of SiO_2 around 1090 cm^{-1}, 800 cm^{-1}, and 460 cm^{-1} corresponding to δ(Si—O—Si), υ(Si—O—Si) and υas(Si—O—Si) vibrations. Bands at 1640 cm^{-1} and 950 cm^{-1} confirmed the presence of residual hydroxyl functions δ(O—H) and υas(Si—OH), respectively. Peaks at the app. 3300 cm^{-1}, 2935 cm^{-1}, and 1610 cm^{-1} corresponded to υ(N—H), $\upsilon_{as}(CH_2\text{-}NH_2)$, and δ(N—H and NH_2) vibrations, respectively [49,50], and confirmed successful functionalization of the silica nanoparticles with the amino-containing ligand AEAM-PTMS.

The surface properties of the particles were changed strongly at each step of surface transformation as revealed by surface charge changes (zeta-potential values) obtained from DLS experiments. The pristine silica nanospheres at pH = 6.5 had a highly negative zeta-potential of − 50.6 mV (±1.18 mV), typical for a hydroxyl-terminated silica. Grafting of a ligand monolayer resulted in recharging of the surface with positive zeta-potential + 9.27 mV (±1.15 mV), emerging apparently due to protonation of the amino functions with formation of positively charged ammonium centers on the surface. Adsorption of Ni^{2+} cations led to recharging with a final negative zeta-potential of − 9.6 mV (±0.369 mV). The positive charge was apparently removed due to complexation of the cations with chelating ligands and formation of close ion pairs as demonstrated by the investigated molecular models (please see part 3.3.1 below for details).

3.2. Adsorption equilibrium isotherms and adsorption kinetics

Fitting of the adsorption data was carried out following Langmuir, Classical Freundlich and Extended Classical Freundlisch, and D-R models [44–46] (see Fig. 4A and S5). The comparison demonstrated that the adsorption isotherms followed the Langmuir model over the concentration range studied for all metals (Fig. 4A), indicating that the adsorption sites were homogeneous and that adsorption of the metal cations proceeded with formation of a monolayer of adsorbate on the uniform material surface with no interactions between adsorbed molecules [51–54]. The AEAM-PTMS ligand as expected, showed affinity towards LTM, due to the existence of two amino donor sites in its structure [55]. Nevertheless, the adsorption capacity for REE was also pronounced. The prepared nanoadsorbent had the highest affinity towards Ni (1.45 mmol/g) and Co (1.18 mmol/g), followed by Sm and Nd (0.56 and 0.47 mmol/g, respectively). Maximum adsorption capacity and metal/ligand stoichiometry results are presented in Table 1. Based on these results, it is possible to conclude that the prepared material, silica grafted with AEAM-PTMS ligand, offered a promising nanoadsorbent for LTM sequestering, obtaining near 1:1 metal to ligand stoichiometry (0.99 for Ni, and 0.80 for Co).

Adsorption kinetics were rapid for all tested metals. The kinetic curves reached equilibrium in 6 h, as seen in Fig. 4B. The adsorption kinetics showed that most of the uptake (70–90 %) occurred within the first 3 h of the interaction of metals with grafted silica nanoparticles. All the kinetics followed pseudo-second-order, which assumes that the metal uptake process is controlled by the adsorption reaction at the liquid/solid interface in the adsorbent and not by diffusion. Comparison of the fitting of pseudo-1st and pseudo-2nd order models [47,48] is presented in Fig. S6.

The mechanism behind metal adsorption onto the surface of the adsorbent is a complex phenomenon and dependent on various factors, such as physico-chemical properties of the metal cations and electrostatic attractions, ionic exchange or complexation (Lewis acid–base interaction) between positively charged metals and negatively charged surfaces of the adsorbent as well as pH of the microenvironment [56–58]. The adsorption isotherm study proved the formation of a monolayer on the surface of the nanoadsorbent and can indicate the chemisorption of targeted metals onto surface functional moieties/

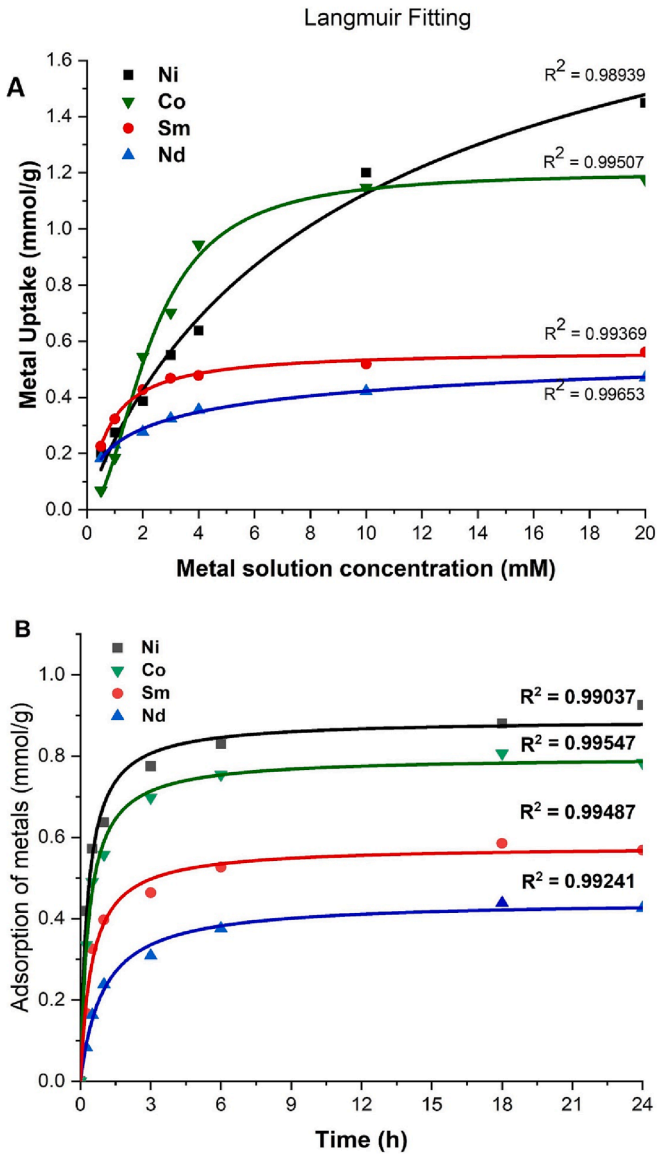

Fig. 4. Adsorption isotherms fitted with Langmuir model (A) and adsorption kinetics fitted with the pseudo-2nd order model (B) of prepared nanoadsorbent material.

Table 1
Maximum adsorption capacities of prepared nanoadsorbent and obtained metal/ligand stoichiometry.

Metal	Maximum adsorption capacities (mmol/g)	Metal/ligand stoichiometry
Co	1.18	0.80
Ni	1.45	0.99
Sm	0.56	0.38
Nd	0.47	0.32

Table 2
Selectivity of prepared nanoadsorbent material.

Metal mixture	Atomic metal ratio
Ni/Co	1/1
Ni/Nd	8.6/1
Co/Sm	3.2/1
Sm/Nd	1.4/1

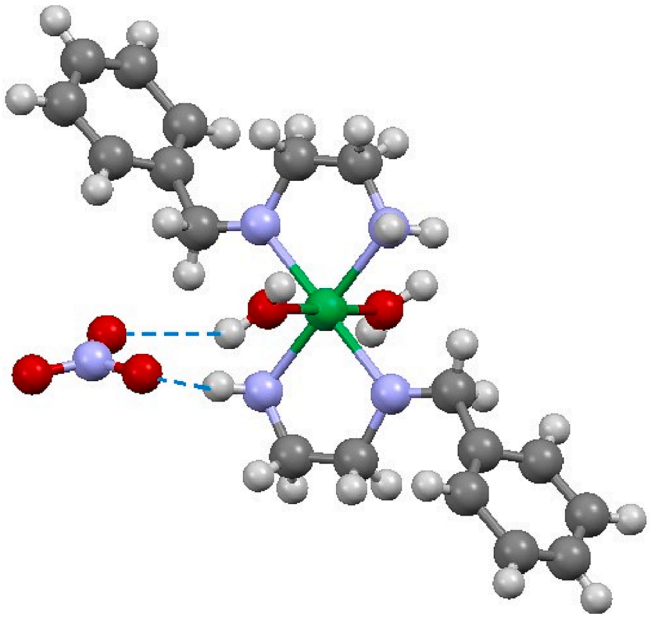

Fig. 5. Molecular structure of the complex $[Ni(\eta 2\text{-}H_2NC_2H_4NHCH_2C_6H_5)_2(H_2O)_2](NO_3)_2$. Only one hydrogen bonded nitrate anion is displayed for clarity.

active sites. Prepared model molecular compounds of metals and ligand in the form of single X-ray quality crystals gave molecular insights into metal complexation (described under 3.3.1).

3.3. Nanoadsorbent selectivity

EDS analysis was used to study average nanoadsorbent selectivity after metal uptake by determining the elemental ratios between metals on different areas of the adsorbents. The results are presented in Table 2. When the adsorbent was used in the mixture of LTM and REE, Ni/Nd, and Co/Sm, the selectivity was 8.6/1 and 3.2/1, respectively. When the adsorbent was tested in an equimolar mixture of two LTMs, the adsorbent did not show selectivity towards Co or Ni. In the case of the equimolar mixture of REE, the adsorbent showed slightly higher selectivity towards Sm. The results show an adsorbent preference to preferentially bind LTM over REE.

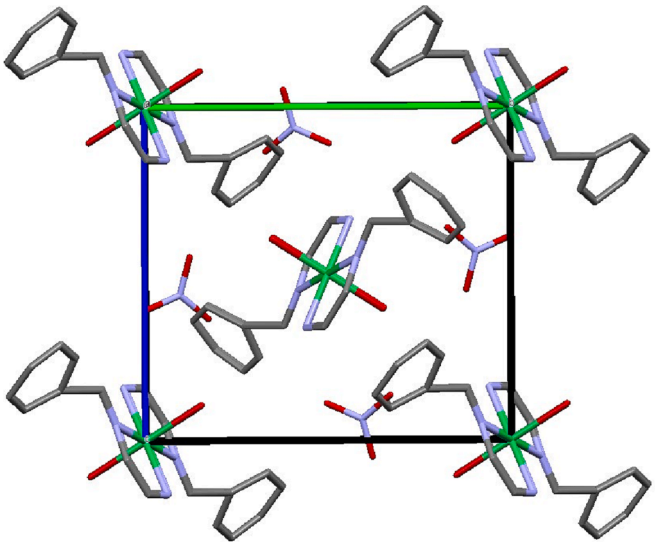

Fig. 6. The packing of $[Ni(\eta 2\text{-}H_2NC_2H_4NHCH_2C_6H_5)_2(H_2O)_2](NO_3)_2$ structural units displayed along the a-axis.

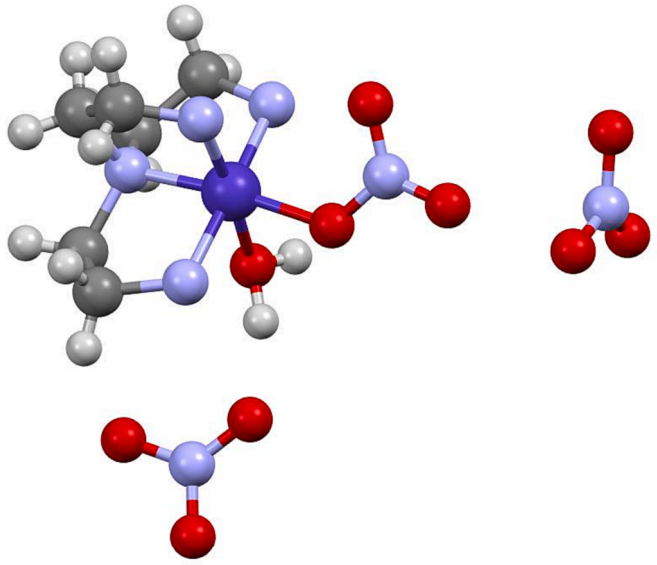

Fig. 7. Molecular structure of the complex $[Co(H_2NC_2H_4)_3N(H_2O)(NO_3)](NO_3)_2$ (**2**).

3.4. Molecular insights into selective action – Crystallographic models

In order to gain better understanding of the observed selective action of the absorbents, we investigated the complex formation between the ligand function, N-aminoethyl-aminomethyl benzene and metal cations. Independent of the applied ratio of reagents, the product turned to be a salt containing a centrosymmetric "propeller-like" cationic unit $[Ni(\eta2\text{-}H_2NC_2H_4NHCH_2C_6H_5)_2(H_2O)_2]^{2+}$ with two ligand molecules attached to the metal cation, along with two nitrate anions connected to the complex via short hydrogen bonding (see Fig. 5). Formation of the complexes with Ni: L = 1: 2 ratio has been reported earlier by Patel et al. [55], but no structural characterization has been provided. Coordination of the nickel cation is octahedral with four nitrogen atoms in the equatorial plane and two hydrating water molecules in the axial positions. The square planar arrangement in this case is apparently not associated with low-spin coordination of Ni(II) or any Jahn-Teller distortion, as the bond length to the nitrogen atoms 2.076(2) and 2.130(2) Å are apparently comparable with the bond length to the solvating water molecules, 2.107(2) Å.

In the crystal structure of the compound, the molecules are aligned with each other as seen from the packing motif (see Fig. 6), but are situated too far from each other for manifestation of π-π stacking – the distance between parallel benzene ring planes being equal to the length of the unit cell parameter, i.e. ca. 10 Å.

The absence of π-π stacking is also revealed via the apparent flipping movement of the benzene rings (see Fig. S2 and S3). In non-restricted refinement, the thermal ellipsoids of carbon atoms in the ring are characteristically elongated. Any attempt of splitting the ring atoms into separate positions for explanation through positional disorder were unsuccessful, making refinement unstable.

In the surface layer, the attachment of Ni^{2+} cations to the ligands should follow the same pattern of chelation, but only one ligand can be bound to the metal centre due to steric reasons. This explains the observed 1: 1 cation-to-ligand stoichiometry. The density of ligand grafting is close to maximum coverage of a smooth silica surface, implying that the separation in space between the ligand molecules should be in the range 6.3–6.8 Å [59]. It should allow better alignment of benzene rings, but is too long for orbital interactions requiring at maximum about 4.4 Å distance between the centroids [60].

No single crystals could be isolated from the Co^{2+} solutions with N-aminoethyl-aminomethyl benzene as ligand, but the color changes (see Fig S4.) indicated rapid oxidation into Co^{3+} species. Since analogous behavior has been observed earlier with a related tris(aminoethyl) amine ligand [40], an attempt to crystallize the cobalt derivative was carried out and successful, resulting in a quantitative yield of the related complex $[Co(H_2NC_2H_4)_3N(H_2O)(NO_3)](NO_3)_2$ (**2**) (see Fig. 7). The Chemistry of Co^{2+} cations in interaction with chelating amino-ligands is discussed in detail in N.N. Greenwood and A. Earnshaw [61], where both the analogies in reactivity and specific stability of $3d^6$ electronic configuration are described and explained.The coordination of the Co^{3+} cation is octahedral with 4 positions occupied by the nitrogen atoms of the ligand, where N(1) provides for the tertiary amino function and N (2), N(3) and N(4) – for the primary amino functions. The residual two places in the inner coordination sphere are occupied by a solvating water molecule O(1) and an oxygen atom of directly bound nitrate anion O(11). An important feature is that all the bonding distances are much shorter compared to Ni^{2+} and are very close to each other except for a considerably longer bond to the solvating water molecule: Co(1)-N(1) 1.919(6), Co(1)-O(11) 1.924(5), Co(1)-N(3) 1.930(12), Co(1)-N(2) 1.938(10), Co(1)-N(4) 1.966(9), and Co(1)-O(1) 1.970(10) Å. This indicates formation of the low-spin $3d^6$ electron configuration, characterized by strong metal–ligand bonding and high activation energy of ligand exchange – a potential hinder for Co_3 + cation desorption at low pH.

Chelating inner sphere complexation of the polyamino ligands with LTM explains the observed affinity of the functionalized adsorbent and hindered desorption of the Co-cations. REE, as demonstrated recently, do not bind to amino functional ligands, but instead can form thin layer deposits of hydroxides [40], making the adsorbent much less efficient to REE compared to LTM.

3.5. Molecular insights into selective action – XPS spectroscopy data

The hybrid adsorbents, as prepared and after uptake of Co, Ni, and Nd, were analyzed by XPS (see Fig. 8). For the Co, Ni, and Nd containing samples, two shifts for N 1 s binding energies were seen, one major at about 400 eV and one minor between 406.2 and 407.3 eV. The minor shift is characteristic of NO_3^-, originating from the $NaNO_3$ used for maintaining the ionic strength during adsorption [62]. The major shift at 398.5 eV for the adsorbent not bearing metal cations (Fig. 8, bottom) corresponds to a protonated amino group [63]. After adsorption of the metal cations, the major N 1 s signal is slightly upshifted with about 1 eV, in good agreement with previous reports of these metal ions in complexation with nitrogen containing ligands [64–66].

High resolution XPS spectra were recorded for all three metal cations. In the case of cobalt cations, as indicated by both the color change on their adsorption and seen from the molecular structure model (Fig. 7), their uptake was associated with oxidation of Co^{2+} into Co^{3+}, and the observed signal at 781 eV corresponded well to the literature data on octahedrally coordinated Co^{3+} cations [67]. In the nickel spectrum, the observed signals at 872.4 and 854.9 eV corresponded well to octahedrally coordinated Ni^{2+} cations [68], which also correlated with the investigated molecular model (Fig. 5). The spectrum of neodymium showed a split peak for Nd^{3+}, indicating potential variety in its coordination. This was expected due to a combination of the surface complexation with the growth of a hydroxide layer caused by the local pH rise via protonation of the amino functions.

3.6. Desorption and reusability study

We tested the desorption efficiency after metal uptake from equimolar metal mixtures of two or four metals. Results were obtained by EDS mapping after samples were shaken for 24 h using four different desorption solutions, HNO_3 with 3 different pH values, and 10 mM EDTA.

Results of metal release after uptake from an equimolar mixture of REE and LTM metal are presented in Fig. 9A for Co/Sm and Fig. 9B for

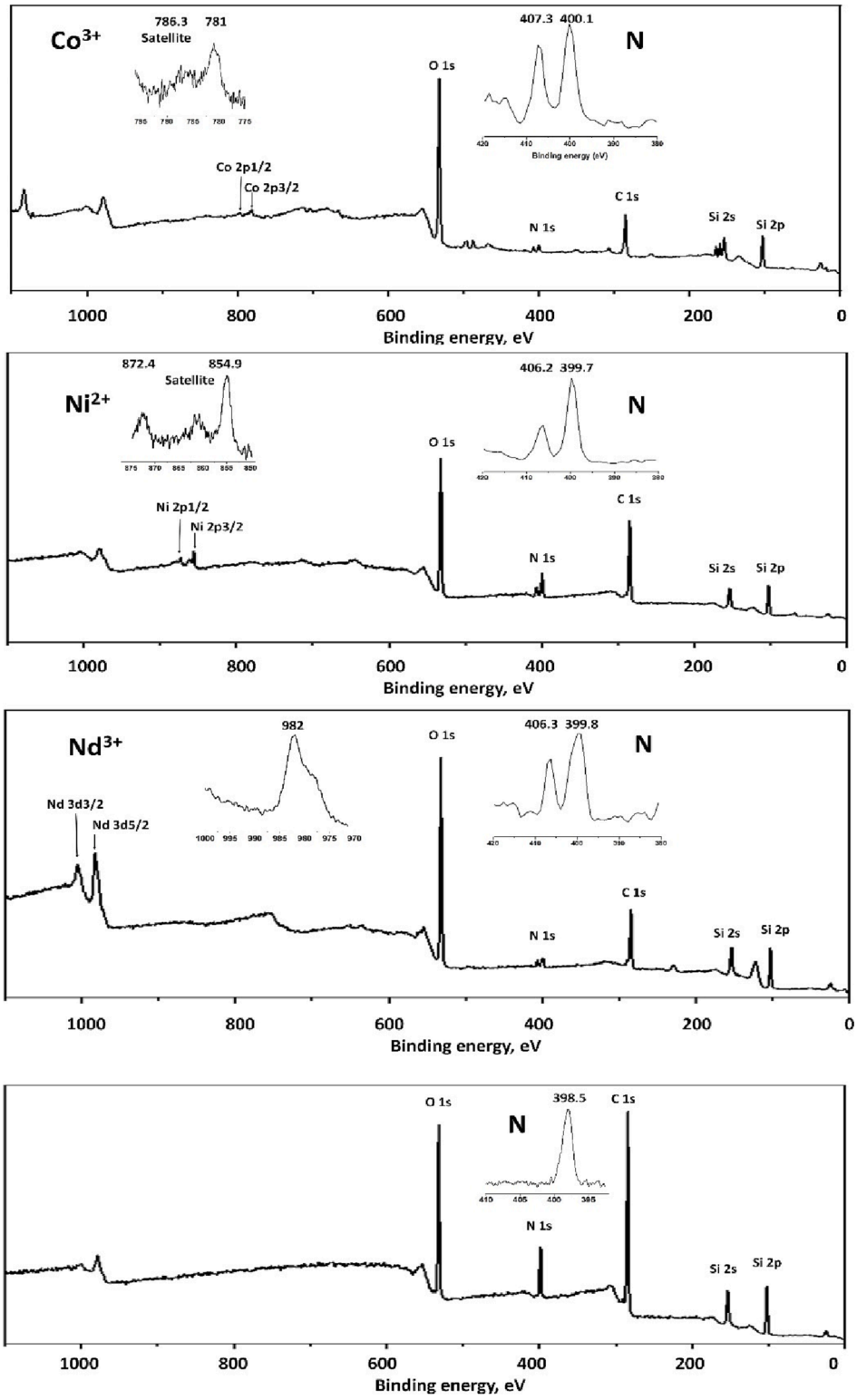

Fig. 8. XPS spectra of the hybrid adsorbent (below) and the adsorbent after uptake of Co, Ni and Nd cations respectively.

Ni/Nd mixture. HNO_3, with the lowest pH value (pH 0), exhibited the highest removal rate of adsorbed Co, while all desorption media removed almost all adsorbed Sm (98–100 %). When the desorption step was repeated using acid with pH 1, the removal rate for Co rose from 52.5 to 75 %. In the case of the Ni/Nd equimolar mixture, the desorption efficiency was high for all metals, varying from 90.5 % (Nd at pH 1) to 100 % (Ni at pH 1). Overall, HNO_3 with pH 0 had the best desorption efficiency. Results of metal release after uptake from an equimolar mixture of LTM cations are presented in Fig. 9C and for the release of REE cations in Fig. 9D. Typically, the Co cations appeared more resilient to acid treatment, as described earlier by our group [40]. This was apparently due to kinetic hinders caused by the crystal field activation energy for the formed Co^{3+} cations with $3d^6$ electron configuration. Characteristically, the desorption efficiency for Ni cations decreases when we try to remove them after uptake from Ni/Co mixtures compared with removal after uptake from mixtures of Ni/Nd. When we

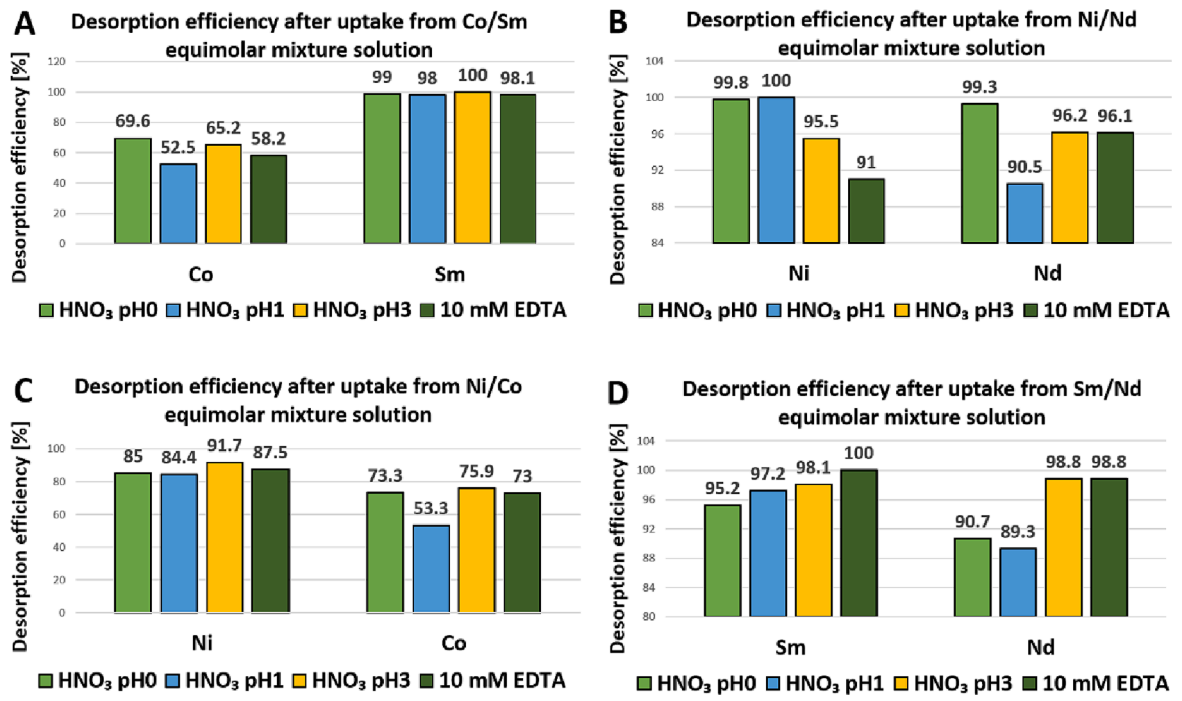

Fig. 9. Desorption efficiency after uptake from two metal equimolar solutions: (A) Co/Sm; (B) Ni/Nd, (C) Ni/Co, and (D) Sm/Nd.

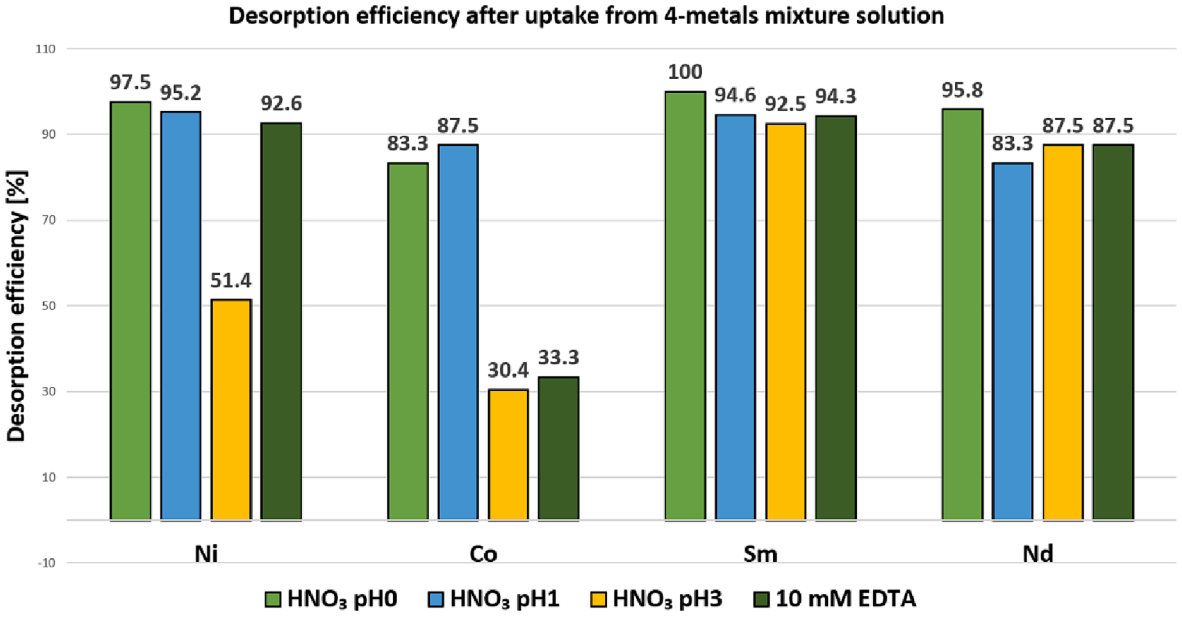

Fig. 10. Desorption efficiency after uptake from a four metal equimolar solution.

Table 3
Nanoadsorbent reusability test study, where A stands for the adsorption step and D for the desorption step.

Metal	1st cycle		2nd cycle		3rd cycle	
	A (mmol/g)	D (%)	A (mmol/g)	D (%)	A (mmol/g)	D (%)
Co	0.750	81.3	0.662	46.2	0.574	67.6
Ni	1.144	100	1.144	92.1	1.100	90
Sm	0.517	97.9	0.474	94.8	0.474	85.6
Nd	0.484	94.1	0.484	100	0.430	90

tried to release the REE cations from Sm/Nd mixtures, the desorption media with higher pH values (i.e. 10 mM EDTA and HNO_3 pH 3) exhibited slightly higher desorption efficiency.

When the desorption efficiency study was carried out after uptake using a four metal mixture, the desorption efficiency was highest using HNO_3 with pH 0 for all metals except for Co (see Fig. 10).

Table 3 shows the possibility of nanoadsorbent reusability. We can observe that samples showed good desorption rates in each cycle ranging between 70——100 %. A decrease in adsorption rates was noted after the first and second desorption cycles for Co. However, the nanoadsorbent had good adsorption/desorption rates even after three cycles for all other metals.

Table 4
Comparison of stability and selectivity between major classes of solid adsorbents with potential capacity to separate LTM from REE.

Matrix	Ligands	Uptake capacity, mmol/g (cation)	Selectivity LTM/REE	References
Silica	Ethylenediamino alkyl Pyridine thioalkyl Thiocyanate Isothiocyanate	1.83 (Co), 1.86(Ni), 1.10(Sm), 0.83(Nd)0.66(Co), 0.55(Ni), 0.56(Sm), 0.50 (Nd)0.75(Co), 0.58 (Ni)0.66(Sm), 0.67 (Nd)0.67(Co), 0.57 (Ni)0.77(Sm), 0.44 (Nd)	Ni/Nd = 5.1/1, Co/Sm = 1/1.65 Ni/Nd = 1/1.78 Co/Sm = 1/12 Ni/Nd = 1/1 Co/Sm = 1/18 Ni/Nd = 1.33/1 Co/Sm = 1/18	[17]
Chitosan&silica	EDTA	0.22(Co), 0.26(Ni)	N/A	[69]
Silica gel	Ni imprinted	0.35(Ni)	N/A	[70]
Zr phosphate	Surface hydrophosphate	0.28–0.56(Eu)	N/A	[71]
ZIF-8/U6N MOF composite	UiO66-NH_2	1.45(Nd)	Co/Nd = 1/2	[72]
ZnBDC MOF	Graphene oxide	2.39(REE general)	N/A	[73]
ZnO	ZnBTC MOF	2.08(REE general)	N/A	[74]
COF	1,3,5-Triformylphloroglucinol (Tp) co-condensed with p-phenylenediamine (Pa)	0.59(La)	N/A	[75]
SBA-15 mesoporous silica	Triethylene pentamine	0.89(Pd) – as potential analog of Ni	N/A	[76]
SBA-15 mesoporous silica	EDTA & alkylphosphonic acid	1.1(Nd)	Ni/Nd = 261.5	[77]
Silica	Ethylenediamino benzene alkyl	1.18(Co), 1.45(Ni), 0.56(Sm), 0.47(Nd)	Ni/Nd = 8.6/1 Co/Sm = 3.2/1	This work

3.7. Comparison with earlier reported adsorbents

The task of separating REE and LTM with focus on LTM separation is of great importance for developing approaches to recycling of magnetic materials, but still remains a relatively scarcely addressed challenge. High selectivity has been proven for mesoporous silica based materials (see Table 4), but they are rather costly and suffer from hinders in desorption of adsorbed components. This emphasizes the need for understanding the principles of constructing adsorbents featuring higher selectivity towards LTM compared to REE. The material reported in the present work combines good adsorption capacity and quick desorption kinetics with pronounced selectivity towards LTM and even considerable difference in behavior between Co and Ni species, which opens new possibilities for many other potential applications.

4. Conclusions

We demonstrated a one-step grafting synthesis of hybrid SiO_2 nanoadsorbents permitting sequestration and separation of REE and LTM – a new and highly requested area of applications. The prepared material was characterized and tested for its adsorption, separation, and reusability properties in single or mixed equimolar metal solutions.

The produced adsorbent showed relatively rapid adsorption kinetics for LTM and REE at room temperature. Adsorption capacity achieved higher values for LTM, demonstrating the formation of surface complexes with 1:1 composition for studied Ni cations. The adsorbent revealed pronounced selectivity towards LTM compared to REE. Molecular insights into the origin of selective action were obtained through studies of the complex formation between the Ni(II) and the N-benzylethylenediamine ligand function and Co(III) with tris(aminoethyl)amine ligand, showing chelation as a principal factor guiding LTM adsorption and desorption. Relatively dense packing of ligands on the silica surface was shown to have potential effects on their ordering permitting high adsorption capacity, resulting in 1:1 cation-to-ligand stoichiometry. The insights obtained from the model molecular structures were supported by the results of the XPS studies.

The desorption of target cations was investigated after uptake from a single metal solution and an equimolar mixture of 2 or 4 metals. The prepared nanoadsorbent exhibits high desorption rates even after three cycles of adsorption and desorption.

To summarize, this work proposes that the evaluated sorbents have potential as an environmentally friendly alternative to the conventional liquid phase separation techniques for LTM separation from REE.

CRediT authorship contribution statement

Troy C. Breijaert: Investigation, Writing – review & editing. **Geoffrey Daniel:** Investigation, Writing – review & editing. **Fredric G. Svensson:** Investigation, Writing – review & editing. **Vadim G. Kessler:** Investigation, Writing – original draft, Writing – review & editing. **Gulaim A. Seisenbaeva:** Conceptualization, Funding acquisition, Supervision, Investigation, Writing – review & editing.

Declaration of Competing Interest

The authors declare that they have no known competing financial interests or personal relationships that could have appeared to influence the work reported in this paper.

Data availability

Data will be made available on request.

Acknowledgments

The authors would like to express gratitude to the ÅForsk foundation, grant No. 21-75, for financial support.

Appendix A. Supplementary material

Supplementary data to this article can be found online at https://doi.org/10.1016/j.seppur.2023.124487.

References

[1] NASA, Global climate change The Causes of Climate Change. Human activities are driving the global warming trend observed since the mid-20th century. https://climate.nasa.gov/causes/#otp_the_role_of_humans, (accessed 15 December 2022).
[2] J. Yu, L.H. Xie, J.R. Li, Y. Ma, J.M. Seminario, P.B. Balbuena, CO_2 Capture and Separations Using MOFs: Computational and Experimental Studies, Chem. Rev. 117 (2017) 9674–9754, https://doi.org/10.1021/acs.chemrev.6b00626.

[3] M. Jowitt, G.M. Mudd, J.F.H. Thompson, Future availability of non-renewable metal resources and the influence of environmental, social, and governance conflicts on metal production, Commun. Earth Environ. 1 (2020) e13.

[4] M. Le Page, The world is warming, and we know why. We also know how to stop it. To stave off the worst effects, we must wean ourselves off greenhouse gas-producing fossil fuels – and fast, hitting "net zero" carbon emissions by mid-century, New Sci. 251 (34–37) (2021) 41–44, https://doi.org/10.1016/S0262-4079(21)01384-1.

[5] T. Kobashi, Y. Choi, Y. Hirano, Y. Yamagata, K. Say, Rapid rise of decarbonization potentials of photovoltaics plus electric vehicles in residential houses over commercial districts, Appl. Energy. 306 (2022), 118142, https://doi.org/10.1016/j.apenergy.2021.118142.

[6] Z. Ye, N. Yu, R. Wei, X.C. Liu, 2022 Decarbonizing regional multi-model transportation system with shared electric charging hubs, Transp. Res. Part C Emerg. Technol. 144 (2022), 103881, https://doi.org/10.1016/j.trc.2022.103881.

[7] B. Ballinger, D. Schmeda-Lopez, B. Kefford, B. Parkinson, M. Stringer, C. Greig, S. Smart, The vulnerability of electric-vehicle and wind-turbine supply chains to the supply of rare-earth elements in a 2-degree scenario, Sustain. Prod. Consum. 22 (2020) 68–76, https://doi.org/10.1016/j.spc.2020.02.005.

[8] G. Bailey, M. Orefice, B. Sprecher, M.A.R. Önal, E. Herraiz, W. Dewulf, K. van Acker, Life cycle inventory of samarium-cobalt permanent magnets, compared to neodymium-iron-boron as used in electric vehicles, J. Cleaner Production. 286 (2021), 125294, https://doi.org/10.1016/j.jclepro.2020.125294.

[9] C. Church, A. Crawford, Green Conflict Minerals: The Fuels of Conflict in the Transition to a Low-carbon Economy, IISD Report, International Institute for Sustainable Development, Manitoba, 2018.

[10] T. Watari, K. Nansai, K. Nakajima, Review of critical metal dynamics to 2050 for 48 elements, Resour. Conserv. Recycl. 155 (2020), 104669, https://doi.org/10.1016/j.resconrec.2019.104669.

[11] W.C. Wilfong, B.W. Kail, Q. Wang, F. Shi, G. Shipley, T.J. Tarka, M.L. Gray, Stable immobilized amine sorbents for heavy metal and REE removal from industrial wastewaters, Environ. Sci.: Water Res. Technol. 6 (2020) 1286–1299, https://doi.org/10.1039/C9EW00915A.

[12] N. Swain, S. Mishra, A review on the recovery and separation of rare earths and transition metals from secondary resources, J. Clean. Prod. 220 (2019) 884–898, https://doi.org/10.1016/j.jclepro.2019.02.094.

[13] M. Gergoric, C. Ekberg, M.R.S.J. Foreman, B.M. Steenari, T. Retegan, Characterization and Leaching of Neodymium Magnet Waste and Solvent Extraction of the Rare-Earth Elements Using TODGA, J. Sustain. Metall. 3 (2017) 638–645, https://doi.org/10.1007/s40831-017-0122-8.

[14] J.Z. Wang, Y.H. Hsieh, Y.C. Tang, Y.H. Shen, Separation of Cobalt, Samarium, Iron, and Copper in the Leaching Solution of Scrap Magnets, Metals 13 (2023) 90, https://doi.org/10.3390/met13010090.

[15] N. Swain, S. Pradhan, S. Mishra, Efficiency of Aliquat 336 for hydrometallurgical separation of Sm (III) and Co (II) from nitrate medium, Miner. Eng. 139 (2019), 105872, https://doi.org/10.1016/j.mineng.2019.105872.

[16] M. Orefice, H. Audoor, Z. Li, K. Binnemans, Solvometallurgical route for the recovery of Sm Co, Cu and Fe from SmCo permanent magnets, Sep. Purif. Technol. 219 (2019) 281–289, https://doi.org/10.1016/j.seppur.2019.03.029.

[17] A. Vardanyan, A. Guillon, T. Budnyak, G.A. Seisenbaeva, Tailoring Nanoadsorbent Surfaces: Separation of Rare Earths and Late Transition Metals in Recycling of Magnet Materials, Nanomater. 12 (2022) 974, https://doi.org/10.3390/nano12060974.

[18] Y. Zhang, F. Gu, Z. Su, S. Liu, C. Anderson, T. Jiang, Hydrometallurgical Recovery of Rare Earth Elements from NdFeB Permanent Magnet Scrap: A Review, Metals. 10 (2020) 841. https://www.mdpi.com/2075-4701/10/6/841.

[19] J. Durain, D. Bourgeois, M. Bertrand, D. Meyer, Comprehensive Studies on Third Phase Formation: Application to $U^{(VI)}/Th^{(IV)}$ Mixtures Extracted by TBP in N-dodecane, Solvent Extr. Ion Exch. 37 (2019) 328–346, https://doi.org/10.1080/07366299.2019.1656853.

[20] F. Xie, T.A. Zhang, D. Dreisinger, F. Doyle, A critical review on solvent extraction of rare earths from aqueous solutions, Min. Eng. 56 (2014) 10–28, https://doi.org/10.1016/j.mineng.2013.10.021.

[21] Y. Hu, J. Florek, D. Larivière, F.-G. Fontaine, F. Kleitz, Recent Advances in the Separation of Rare Earth Elements Using Mesoporous Hybrid Materials, Chem. Rec. 18 (2018) 1261–1276, https://doi.org/10.1002/tcr.201800012.

[22] X. Vecino, M. Reig, Wastewater Treatment by Adsorption and/or Ion-Exchange Processes for Resource Recovery, Water. 14 (2022) 911, https://doi.org/10.3390/w14060911.

[23] J. Florek, A. Mushtaq, D. Lariviere, G. Cantin, F.-G. Fontaine, F. Kleitz, Selective recovery of rare earth elements using chelating ligands grafted on mesoporous surfaces, RSC Adv. 5 (2015) 103782–103789, https://doi.org/10.1039/C5RA21027E.

[24] J.C. Callura, K.M. Perkins, C.W. Noack, N.R. Washburn, D.A. Dzombak, A. K. Karamalidis, Selective adsorption of rare earth elements onto functionalized silica particles, Green Chem. 20 (2018) 1515–1526, https://doi.org/10.1039/C8GC00051D.

[25] A. Hadela, M. Lakic, M. Potocnik, A. Kosak, A. Gutmaher, A. Lobnik, Novel reusable functionalized magnetic cobalt ferrite nanoparticles as oil adsorbents, Adsorp Sci Technol. 38 (2020) 168–190, https://doi.org/10.1177/0263617420922014.

[26] H. Zhang, Y. Pan, Z. Wang, A. Wu, Y. Zhang, Synthesis of hollow mesoporous manganese dioxide nanoadsorbents with strong negative charge and their ultra-efficient adsorption for cationic dyes, Sep. Purif. Technol. 295 (2022), 121241, https://doi.org/10.1016/j.seppur.2022.121241.

[27] P. Moharrami, E. Motamedi, Application of cellulose nanocrystals prepared from agricultural wastes for synthesis of starch-based hydrogel nanocomposites: Efficient and selective nanoadsorbent for removal of cationic dyes from water, Bioresour. Technol. 313 (2020), 123661, https://doi.org/10.1016/j.biortech.2020.123661.

[28] P. Pillai, S. Dharaskar, M. Shah, R. Sultania, Determination of fluoride removal using silica nano adsorbent modified by rice husk from water, Groundw. Sustain. Dev. 11 (2020), 100423, https://doi.org/10.1016/j.gsd.2020.100423.

[29] M.E. Peralta, D.O. Mártire, M.S. Moreno, M.E. Parolo, L. Carlos, Versatile nanoadsorbents based on magnetic mesostructured silica nanoparticles with tailored surface properties for organic pollutants removal, J. Environ. Chem. Eng. 9 (2021), 104841, https://doi.org/10.1016/j.jece.2020.104841.

[30] S. Das, A. Samanta, K. Kole, G. Gangopadhyay, S. Jana, MnO_2 flowery nanocomposites for efficient and fast removal of mercury(ii) from aqueous solution: a facile strategy and mechanistic interpretation, Dalton Trans. 49 (2020) 6790–6800, https://doi.org/10.1039/D0DT01054E.

[31] M. Kalantari, Z. Gu, Y. Cao, C. Lei, J. Zhang, Thiolated silica nanoadsorbents enable ultrahigh and fast decontamination of mercury(II): understanding the contribution of thiol moieties' density and accessibility on adsorption performance, Environ. Sci.: Nano. 7 (2020) 851–860, https://doi.org/10.1039/C9EN01123D.

[32] I. Ali, M. Asim, T.A. Khan, Low cost adsorbents for the removal of organic pollutants from wastewater, J Environ. Manage. 113 (2012) 170–183, https://doi.org/10.1016/j.jenvman.2012.08.028.

[33] S.P. Mishra, Adsorption–desorption of heavy metal ions, Current Science, 107 (2014) 601-612. JSTOR, http://www.jstor.org/stable/24103532, 2014 (Accessed 7 December 2022).

[34] B.I. Kharisov, H.V.R. Dias, O.V. Kharissova, Nanotechnology-based remediation of petroleum impurities from water, J. Pet. Sci. Eng. 122 (2014) 705–718, https://doi.org/10.1016/j.petrol.2014.09.013.

[35] Y. Wu, H. Pang, Y. Liu, X. Wang, S. Yu, D. Fu, X. Wang, Environmental remediation of heavy metal ions by novel-nanomaterials: A review, Environ. Pollut. 246 (2019) 608–620, https://doi.org/10.1016/j.envpol.2018.12.076.

[36] F. Almomani, R. Bhosale, M. Khraisheh, A. Kumar, T. Almomani, Heavy metal ions removal from industrial wastewater using magnetic nanoparticles (MNP), Appl. Surf. Sci. 506 (2020), 144924, https://doi.org/10.1016/j.apsusc.2019.144924.

[37] H. Sadegh, G.A.M. Ali, Potential Applications of Nanomaterials in Wastewater Treatment: Nanoadsorbents Performance, in: A. Hussain, S. Ahmed (Eds.), Advanced Treatment Techniques for Industrial Wastewater, IGI Global, Hershey, 2019, pp. 51–61.

[38] H. Irving, J.M.M. Griffiths, The stabilities of complexes formed by some bivalent transition metals with N-alkyl-substituted ethylenediamines, J. Chem. Soc. (1954) 213–223, https://doi.org/10.1039/JR9540000213.

[39] P. Paoletti, Formation of metal complexes with ethylenediamine: a critical study of equilibrium constants, enthalpy and entropy values, Pure & Appl. Chem. 56 (1984) 491–522, https://doi.org/10.1351/pac198456040491.

[40] T.C. Breijaert, T.M. Budnyak, V.G. Kessler, G.A. Seisenbaeva, Tailoring a bio-based adsorbent for sequestration of late transition and rare earth elements, Dalton Trans. 51 (2022) 17978–17986, https://doi.org/10.1039/D2DT03150G.

[41] E. Polido Legaria, M. Samouhos, V.G. Kessler, G.A. Seisenbaeva, Toward Molecular Recognition of REEs: Comparative Analysis of Hybrid Nanoadsorbents with the Different Complexonate Ligands EDTA, DTPA, and TTHA, Inorg. Chem. 56 (2017) 13938–13948, https://doi.org/10.1021/acs.inorgchem.7b02056.

[42] M. Barczak, Functionalization of mesoporous silica surface with carboxylic groups by Meldrum's acid and its application for sorption of proteins, J. Porous Mater. 26 (2019) 291–300, https://doi.org/10.1007/s10934-018-0655-7.

[43] N. Fairley, V. Fernandez, M. Richard-Plouet, C. Guillot-Deudon, J. Walton, E. Smith, D. Flahaut, M. Greiner, M. Biesinger, S. Tougaard, D. Morgan, J. Baltrusaitis, Appl. Surf. Sci. Adv. 5 (2021), 100112.

[44] K.Y. Foo, B.H. Hameed, Insight into the modeling of adsorption isotherm systems, Chem. Eng. J. 156 (2010) 2–10, https://doi.org/10.1016/j.cej.2009.09.013.

[45] S. Kundu, A.K. Gupta, Arsenic adsorption onto iron oxide-coated cement (IOCC): regression analysis of equilibrium data with several isotherm models and their optimization, Chem. Eng. J. 122 (2006) 93–106, https://doi.org/10.1016/j.cej.2006.06.002.

[46] R. Flatt, I. Schober, Superplasticizers and the rheology of concrete, in: N. Roussel (Ed.), Understanding the Rheology of Concrete, Woodhead Publishing Limited, Sawston, 2012, pp. 144–208.

[47] L. Largitte, R. Pasquier, A review of the kinetics adsorption models and their application to the adsorption of lead by an activated carbon, Chem. Eng. Res. Des. 109 (2016) 495–504, https://doi.org/10.1016/j.cherd.2016.02.006.

[48] T.R. Sahoo, B. Prelot, Adsorption processes for the removal of contaminants from wastewater, in: B. Bonelli, F.S. Freyria, I. Rossetti, R. Sethi (Eds.), Nanomaterials for the Detection and Removal of Wastewater Pollutants (Book), Elsevier Inc., Amsterdam, 2020, pp. 161–222.

[49] G. Socrates, Infrared and Raman Characteristic Group Frequencies, Tables and Charts, third ed., John Wiley and Sons, Chichester, 2004.

[50] B. Stuart, Infrared Spectroscopy: Fundamentals and Applications, John Wiley & Sons, Sydney, 2004.

[51] I. Langmuir, The Constitution and Fundamental Properties of Solids and Liquids. Part I. Solids, J. Am. Chem. Soc. 38 (1916) 2221–2295, https://doi.org/10.1021/ja02268a002.

[52] I. Langmuir, The Adsorption of Gases on Plane Surfaces of Glass, Mica and Platinum, J. Am. Chem. Soc. 40 (1918) 1361–1403, https://doi.org/10.1021/ja02242a004.

[53] H. Swenson, N.P. Stadie, Langmuir's Theory of Adsorption: A Centennial Review, Langmuir. 35 (2019) 5409–5426, https://doi.org/10.1021/acs.langmuir.9b00154.

[54] S. Alafnan, A. Awotunde, G. Glatz, S. Adjei, I. Alrumaih, A. Gowida, Langmuir adsorption isotherm in unconventional resources: Applicability and limitations, J. Pet. Sci. Eng. 207 (2021), 109172, https://doi.org/10.1016/j.petrol.2021.109172.
[55] K.C. Patel, D.E. Goldberg, Aralkylpolyamine complexes—VI: Complexes of nickel (II) with N-benzylethylenediamine, J. inorg. nucl. chem. 36 (1974) 565–568, https://doi.org/10.1016/0022-1902(74)80114-4.
[56] R. Garg, R. Garg, N.O. Eddy, A.I. Almohana, S.F. Almojil, M.A. Khan, S.H. Hong, Biosynthesized silica-based zinc oxide nanocomposites for the sequestration of heavy metal ions from aqueous solutions, J. King Saud Univ. Sci. 34 (2022), 101996, https://doi.org/10.1016/j.jksus.2022.101996.
[57] X. Fan, H. Liu, E. Anang, D. Ren, Effects of electronegativity and hydration energy on the selective adsorption of heavy metal ions by synthetic NaX zeolite, Materials. 14 (2021) 4066, https://doi.org/10.3390/ma14154066.
[58] X. Xin, Q. Wei, J. Yang, L. Yan, R. Feng, G. Chen, B. Du, H. Li, Highly efficient removal of heavy metal ions by amine-functionalized mesoporous Fe_3O_4 nanoparticles, Chem. Eng. J. 184 (2012) 132–140, https://doi.org/10.1016/j.cej.2012.01.016.
[59] E. Polido Legaria, S. Demirel Topel, V.G. Kessler, G.A. Seisenbaeva, Molecular insights into selective action of a magnetically removable complexone-grafted adsorbent, Dalton Trans. 44 (2015) 1273–1282, https://doi.org/10.1039/C4DT03096F.
[60] S. Alvarez, A cartography of the van der Waals territories, Dalton Trans. 42 (2013) 8617–8636, https://doi.org/10.1039/C3DT50599E.
[61] N.N. Greenwood, A. Earnshaw, Chemistry of the Elements ch. 26 (1986) 1116–1117.
[62] J. Baltrusaitis, P.M. Jayaweera, V.H. Grassian, XPS study of nitrogen dioxide adsorption on metal oxide particle surfaces under different environmental conditions, Phys. Chem. Chem. Phys. 11 (2009) 8295–8305, https://doi.org/10.1039/B907584D.
[63] A. Artemenko, A. Shchukarev, P. Štenclová, T. Wågberg, J. Segervald, X. Jia, A. Kromka, Reference XPS spectra of amino acids, IOP Conf. Series: Materials Sci. Eng. 1050 (2021), 012001, https://doi.org/10.1088/1757-899X/1050/1/012001.
[64] K.C. Dash, B. Folkesson, R. Larsson, M. Mohapatra, An Xps Investigation On A Series Of Schiff Base Dioxime Ligands And Cobalt Complexes, J. Electron Spectrosc. Related Phenomena 49 (1989) 343–357, https://doi.org/10.1016/0368-2048(89)85022-4.
[65] A.R. Silva, M. Martins, M.M.A. Freitas, A. Valente, C. Freire, B. de Castro, J. L. Figueiredo, Immobilisation of amine-functionalised nickel(II) Schiff base complexes onto activated carbon treated with thionyl chloride, Microporous Mesoporous Mater. 55 (2002) 275–284, https://doi.org/10.1016/S1387-1811(02)00429-8.
[66] D. Lionetti, V.W. Day, J.D. Blakemore, Noncovalent immobilization and surface characterization of lanthanide complexes on carbon electrodes, Dalton Trans. 46 (2017) 11779–11789, https://doi.org/10.1039/C7DT02577G.
[67] Q.L. Yang, D. Wang, C.Z. Wang, X.F. Li, K.Z. Li, Y. Peng, J.H. Li, Facile surface improvement method for $LaCoO_3$ for toluene oxidation, Catal. Sci. Technol. 8 (2018) 3166–3173, https://doi.org/10.1039/C8CY00765A.
[68] A.P. Grosvenor, M.C. Biesinger, R.St.C. Smart, N.S. McIntyre, New interpretations of XPS spectra of nickel metal and oxides, Surface Sci. 600 (2006) 1771–1779. https://doi.org/10.1016/j.susc.2006.01.041.
[69] E. Repo, J.K. Warchoł, A. Bhatnagar, M. Sillanpää, Heavy metals adsorption by novel EDTA-modified chitosan–silica hybrid materials, J Colloid Interface Sci 358 (2011) 261–267, https://doi.org/10.1016/j.jcis.2011.02.059.
[70] H.X. He, Q. Gan, C.G. Feng, Preparation and application of Ni(II) ion-imprinted silica gel polymer for selective separation of Ni(II) from aqueous solution, RSC Adv. 7 (2017) 15102–15111, https://doi.org/10.1039/C7RA00101K.
[71] J. Veliscek-Carolan, T.L. Hanley, V. Luca, Zirconium organophosphonates as high capacity, selective lanthanide sorbents, Separation Purif. Technol. 129 (2014) 150–158, https://doi.org/10.1016/j.seppur.2014.03.028.
[72] M.M. Zhang, K. Yang, J.S. Cui, H.B. Yu, Y.J. Wang, W.J. Shan, Z.N. Lou, Y. Xiong, 3D-agaric like core-shell architecture UiO-66-NH2@ZIF-8 with robust stability for highly efficient REEs recovery, Chem Eng J 386 (2020) 124023, https://doi.org/10.1016/j.cej.2020.124023.
[73] Z.Y. Chen, Z. Li, J. Chen, H.X. Tan, J.S. Wu, H.D. Qiu, Selective Adsorption of Rare Earth Elements by Zn-BDC MOF/Graphene Oxide Nanocomposites Synthesized via In Situ Interlayer-Confined Strategy, Ind. Eng. Chem. Res. 61 (2022) 1841–1849, https://doi.org/10.1021/acs.iecr.1c04180.
[74] J.S. Wu, Z. Li, H.X. Tan, S.B. Du, T.Q. Liu, Y.L. Yuan, X.H. Liu, H.D. Qiu, Highly Selective Separation of Rare Earth Elements by Zn-BTC Metal−Organic Framework/Nanoporous Graphene via In Situ Green Synthesis, Anal. Chem. 93 (2021) 1732–1739, https://doi.org/10.1021/acs.analchem.0c04407.
[75] J. Xiao, B. Li, R.B. Qiang, H.D. Qiu, J. Chen, Highly selective adsorption of rare earth elements by honeycomb-shaped covalent organic frameworks synthesized in deep eutectic solvents, Environ. Res. 214 (2022), 113977, https://doi.org/10.1016/j.envres.2022.113977.
[76] S.Z. Xu, S.Y. Ning, Y.B. Wang, X.P. Wang, H.R. Dong, L.F. Chen, X.B. Yin, T. Fujita, Y.Z. Wei, Precise separation and efficient enrichment of palladium from wastewater by amino-functionalized silica adsorbent, J. Cleaner Prod. 396 (2023), 136479, https://doi.org/10.1016/j.jclepro.2023.136479.
[77] O. Dudarko, N. Kobylinska, V. Kessler, G. Seisenbaeva, Recovery of rare earth elements from NdFeB magnet by mono- and bifunctional mesoporous silica: Waste recycling strategies and perspectives, Hydrometallurgy 210 (2022), 105855, https://doi.org/10.1016/j.hydromet.2022.105855.